
Article:
Yang, M. orcid.org/0000-0002-9993-6313, Defillion, J., Scarpa, F. et al. (1 more author) (2023) Volume optimisation of multi-stable origami bellows for deployable space habitats. Acta Mechanica Solida Sinica, 36. pp. 514-530. ISSN 0894-9166

https://doi.org/10.1007/s10338-023-00401-3

Acta Mechanica Solida Sinica (2023) 36:514–530
https://doi.org/10.1007/s10338-023-00401-3

Volume Optimisation of Multi-stable Origami Bellows for Deployable Space Habitats

Mengzhu Yang[1] · Joe Defillion[1] · Fabrizio Scarpa[1] · Mark Schenk[1]

Received: 17 February 2023 / Revised: 11 May 2023 / Accepted: 14 May 2023 / Published online: 23 June 2023

Abstract
Origami bellows are formed by folding flat sheets into closed cylindrical structures along predefined creases. As the bellows unfold, the volume of the origami structure will change significantly, offering potential for use as inflatable deployable structures. This paper presents a geometric study of the volume of multi-stable Miura-ori and Kresling bellows, focusing on their application as deployable space habitats. Such habitats would be compactly stowed during launch, before expanding once in orbit. The internal volume ratio between different deployed states is investigated across the geometric design space. As a case study, the SpaceX Falcon 9 payload fairing is chosen for the transportation of space habitats. The stowed volume and effective deployed volume of the origami space habitats are calculated to enable comparison with conventional habitat designs. Optimal designs for the deployment of Miura-ori and Kresling patterned tubular space habitats are obtained using particle swarm optimisation (PSO) techniques. Configurations with significant volume expansion can be found in both patterns, with the Miura-ori patterns achieving higher volume expansion due to their additional radial deployment. A multi-objective PSO (MOPSO) is adopted to identify trade-offs between volumetric deployment and radial expansion ratios for the Miura-ori pattern.

Keywords Optimisation · Origami bellows · Space habitat · Origami volume

1 Introduction

Origami is a traditional Japanese paper art that forms flat sheets into three-dimensional objects by folding along predefined creases. Due to its stowability, deployability, and programmable stiffness, origami has been applied in many fields ranging from the micro-/nanometre scale to the metre scale [1], such as nano-photonics [2] and inflatable shelters [3].

Origami bellows [4] are created by folding planar origami patterns into closed hollow cylindrical structures; these include the Miura-ori [5], Kresling [6], and waterbomb [7] patterns. Such bellows are shown to have rich mechanical properties including multi-stability [5, 8, 9], self-locking behaviour [10, 11], and tunable stiffness [12–14]. As such, origami bellows have been applied in fields such as robotics [15, 16], meta-materials [17, 18], binary switch [19], and self-folding structures [20–22]. Origami bellows are promising candidates for self-folding inflatable structures since the structure itself serves as the inflatable chamber. Inflation actuation utilises the pressure of compressed air or fluid to trigger the deformation of origami. For instance, Li et al. [23] introduced fluid-driven origami-inspired artificial muscles that can be programmed to achieve multi-axial motions including contraction, bending, and torsion. Melancon et al. [3] designed several bistable origami units that can be deployed through a single fluidic pressure input and combined these units to build functional structures at the metre scale. Melancon et al. [24] also used pressure to trigger a snap-through transition of a multi-stable Kresling. The inflatable origami may experience a significant volume change during the deployment process. Zhang et al. [25] approximated the volume of Kresling by assuming that the cross section of the oblique polygonal prism is constant. However, the actual volume change of inflatable origami has rarely been studied.

Inflatable origami structures have been proposed for aerospace applications due to their high deployment ratio, low system complexity and simple deployment mechanism

✉ Mengzhu Yang
mengzhu.yang@bristol.ac.uk

[1] Department of Aerospace Engineering, University of Bristol, Bristol BS8 1TR, UK

[26]. The structure can be manufactured on Earth, folded into a compact configuration for launch and expanded to a larger volume once in orbit. Of particular interest is the use of origami concepts in deployable space habitats. Space habitats are where humans live in outer space and thus, need to withstand extreme space environments (e.g., radiation, meteoroids, and orbital debris). Deployable structures could significantly increase the amount of usable volume of space station modules [27] or habitats on the lunar surface. For example, the Bigelow Expandable Activity Module (BEAM) [28] has been successfully launched and expanded once docked to the International Space Station (ISS). Origami concepts such as the Miura-ori [29], accordion [27], Kresling, and Tachi-Miura polyhedron (TMP) fold patterns [30] have been considered for deployable habitats. For instance, the LUNARK habitat mission created a lunar habitat based on the Miura-ori pattern with a rigid carbon fibre shell, which can reach a volume expansion of 750% [29]. Morgan et al. [27] introduced a habitat using a modified accordion fold pattern accounting for material thickness, which has an 85% increase in length and volume between the stowed and expanded configurations. Yasuda et al. [30] designed volumetric origami cells made of TMP that can exhibit in-situ transition between flat-foldable and load-bearing states without modifying their predefined crease patterns or hitting the kinematically singular configuration. However, it is difficult to fairly compare the origami habitats to conventional habitat modules since they are irregular-shaped. Moreover, optimal design of origami-based space habitats has rarely been investigated.

In this work, we focus on two widely applied origami bellow patterns—Kresling and Miura-ori—and evaluate their potential as deployable space habitats. The remainder of the paper is organised as follows. Section 2 describes the crease patterns and internal volume calculation for bistable Miura-ori and tristable Kresling bellows. A study on the volume ratio between different stable states is presented. To compare the performance of origami habitats to conventional habitat modules, the definition and calculation of effective volume of origami space habitats are introduced in Sect. 3. Next, optimisation methods are used to find patterns with high volume deployment ratio, whilst trading off against radial expansion. The findings of this paper are concluded in Sect. 4.

2 Crease Patterns and Volume Calculations

2.1 Miura-ori

The crease pattern and three-dimensional model of two-layer Miura-ori bellows are illustrated in Fig. 1. The pattern can be described by sector angles ϕ_1 and ϕ_2, vertex spacing d_1 and d_2, radius R, layer height H, number of unit cells around the circumference n and number of layers along the length of the bellows m. A single unit cell consists of two adjacent facets, as highlighted in Fig. 1a. For Miura-ori bellows, ϕ_1 and ϕ_2 satisfy:

$$0 < \phi_2 < \phi_1 < \frac{\pi}{2} \tag{1}$$

and

$$d_1 + d_2 = \frac{2\pi R}{n} \tag{2}$$

Following Reid et al. [5], to form closed bellows, a cylindrical closure condition is introduced:

$$\theta_2 = \pi - \frac{2\pi}{n} - \theta_1 \tag{3}$$

with

$$\tan\frac{\theta_1}{2} = \frac{1}{2\tan\frac{\pi}{n}}\left[1 - \frac{\tan\phi_2}{\tan\phi_1} - \sqrt{\left(\frac{\tan\phi_2}{\tan\phi_1} - 1\right)^2 - 4\frac{\tan\phi_2}{\tan\phi_1}\tan^2\frac{\pi}{n}}\right] \tag{4}$$

where θ_1 and θ_2 are angles defined in Fig. 1b. Next, the angle ψ can be calculated as follows:

$$\psi = \frac{\pi}{2} - \arcsin\left(\frac{\tan\frac{\theta_1}{2}}{\tan\phi_2}\right) \tag{5}$$

which represents the folded state of the bellows, with $\psi = 0$ representing a flat-folded configuration. The parameter d_2 and the layer height H are geometrically restricted to [5]:

$$0 < H \leq \frac{2\pi R/n - d_2}{\cot\phi_2 - \cot\phi_1} \tag{6}$$

Thus, the geometric design parameters are given by ϕ_1, ϕ_2, R, d_1, H, m, and n, whilst the remaining parameters can be calculated. The 3D geometry such as the positions of the vertices can be calculated using the SO(3) rotation matrices method proposed by Reid et al. [5]. Moreover, when the vertex spacing $d_2 = 0$, the Miura-ori pattern reduces to the Kresling pattern.

2.1.1 Bistability

To satisfy Eqs. (4) and (5), ϕ_1 and ϕ_2 (or ϕ_1' and ϕ_2') should be in the region bounded by [5]:

$$g_1(\phi_1, n) = \phi_1 - \frac{\pi}{n} \quad (\text{flat} - \text{foldable line}) \tag{7}$$

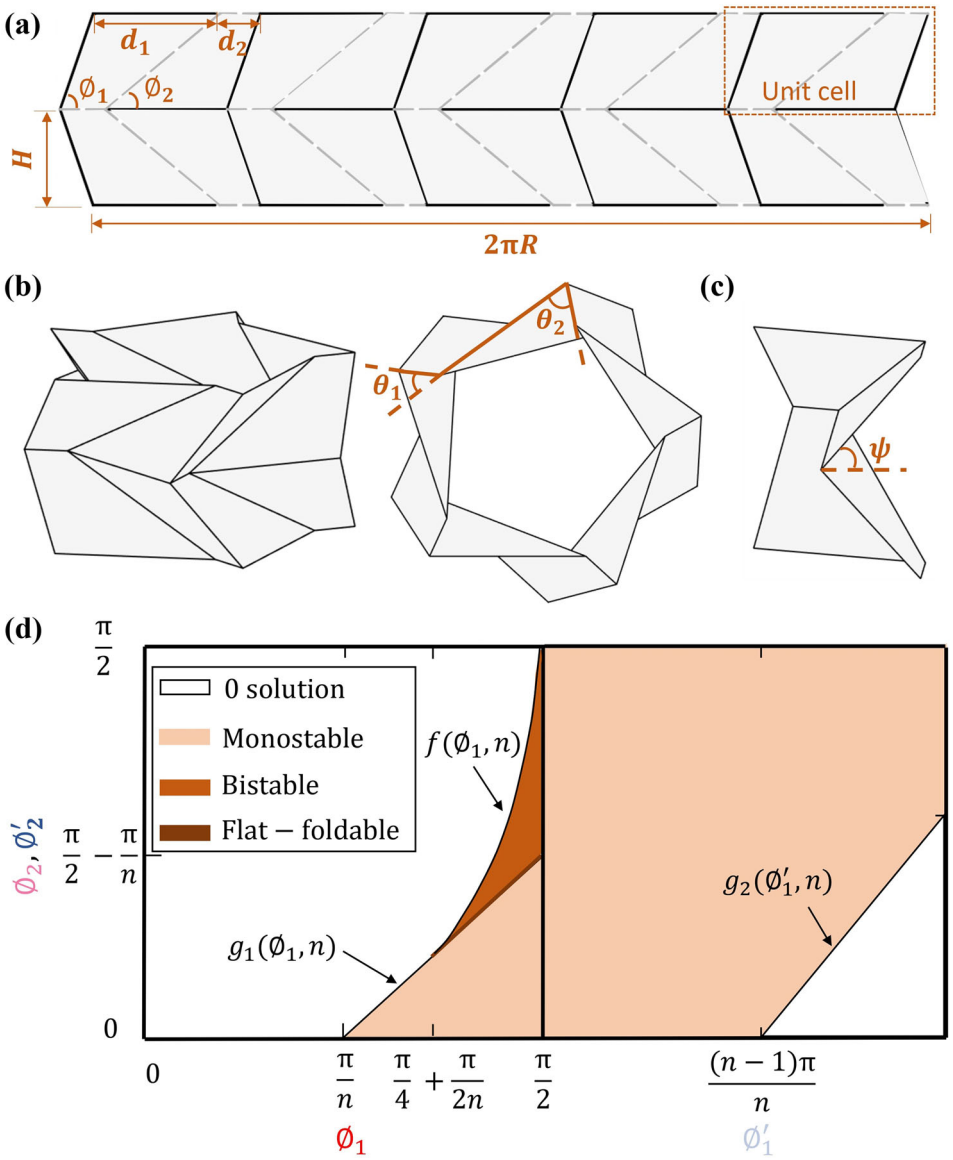

Fig. 1 Geometry of Miura-ori bellows and geometric design space. **a** Crease pattern of two-layer Miura-ori bellows, with sector angles ϕ_1 and ϕ_2, crease lengths d_1 and d_2, bellow radius R, facet height H, number of unit cells around the circumference n, and number of layers along the length of the bellows m (here $n = 5$, $m = 2$); for $d_2 = 0$, the Kresling pattern is recovered. The solid lines represent mountain folds, while the dashed lines represent valley folds. **b** Assembled Miura-ori bellows, where θ_1 and θ_2 are angles between two adjacent folds along the circumference. **c** Two adjacent unit cells in folded state, where 2ψ is the dihedral angle between adjacent facets. **d** The geometric design space (modified from [5]) indicating the invalid, monostable and bistable regions, where $\phi_1^{'}$ and $\phi_2^{'}$ are sector angles of Kresling at the third stable state S_3, which will be introduced in Sect. 2.2.1

$$f(\phi_1, n) = \arctan\left(\tan(\phi_1)\frac{1-\sin\left(\frac{\pi}{n}\right)}{1+\sin\left(\frac{\pi}{n}\right)}\right) \tag{8}$$

$$g_2\left(\phi_1^{'}, n\right) = \phi_1^{'} - \pi + \frac{\pi}{n} \tag{9}$$

The design space of the bellows can therefore be divided into three regions [5]: (i) invalid parameters, (ii) monostable region, and (iii) bistable region (including the flat-foldable line), as illustrated in Fig. 1d. Note that this definition of multi-stability does not depend on strain energy considerations, but rather geometric compatibility. Crucially, for the deployment between stable states, the origami structure must deform through bending and stretching of the facets—this is not modelled in this work. Here, we exploit the multi-stability of the origami bellows to provide compatible configurations for both the stowed and deployed configurations.

2.1.2 Volume Calculation

The volume of Miura-ori bellows can be calculated using the Cartesian coordinate positions of the vertices of a single unit in 3D space (as shown in Fig. 2) and then, multiplying by mn. Each single unit can be divided into six tetrahedra, namely $B_0B_1B_2A_1$, $B_0B_2B_3A_3$, $B_0B_3A_2A_3$, $B_0B_2A_1A_2$, $B_0A_0A_2A_3$, and $B_2A_0A_1A_2$, as shown in Fig. 2. Sharing the same height and base area, $V_{B_0B_1B_2A_1} = V_{B_0A_0A_2A_3}$, and $V_{B_0B_2B_3A_3} = V_{B_2A_0A_1A_2}$. Thus, the total volume can be expressed as follows:

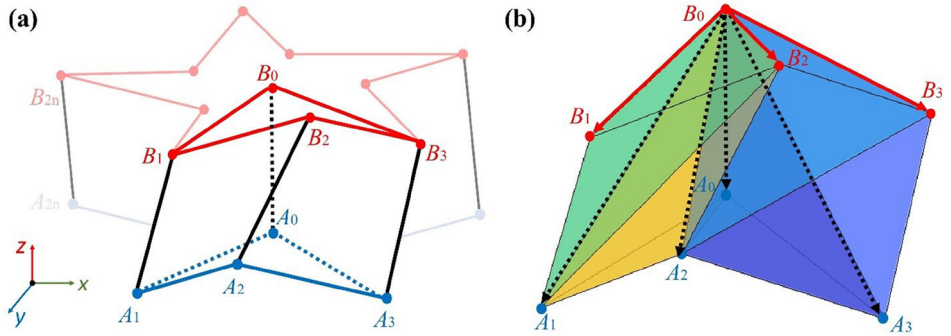

Fig. 2 Geometry and volume calculation of Miura-ori bellows. **a** 3D view of the geometry of a single unit cell in one-layer Miura-ori bellows, where A_0B_0 is the cylinder axis of the bellows parallel to the z-axis. **b** The volume of a unit cell represented by the combination of six tetrahedra ($B_0B_1B_2A_1$, $B_0B_2B_3A_3$, $B_0B_3A_2A_3$, $B_0B_2A_1A_2$, $B_0A_0A_2A_3$, and $B_2A_0A_1A_2$) displayed by shaded areas, where the vectors used to calculate the volume using Eq. (10) are highlighted

$$V_M = mn\Big(\frac{1}{3}(\boldsymbol{B_0B_1}\times\boldsymbol{B_0B_2})\cdot\boldsymbol{B_0A_1} + \frac{1}{3}(\boldsymbol{B_0B_2}\times\boldsymbol{B_0B_3})\cdot\boldsymbol{B_0A_3}\ldots + \frac{1}{6}(\boldsymbol{B_0B_3}\times\boldsymbol{B_0A_2})\cdot\boldsymbol{B_0A_3} + \frac{1}{6}(\boldsymbol{B_0B_2}\times\boldsymbol{B_0A_1})\cdot\boldsymbol{B_0A_2}\Big) \tag{10}$$

where $\boldsymbol{B_iB_j}$ is the vector from B_i to B_j, and $\boldsymbol{B_iA_j}$ is the vector from B_i to A_j, as highlighted in Fig. 2.

2.2 Kresling

The Kresling pattern can be derived straightforwardly from the Miura-ori pattern by setting the vertex spacing d_2 equal to zero. The prediction of multi-stability only depends on sector angles ϕ_1 and ϕ_2, and thus, the design space is the same for normal Kresling and Miura-ori patterns (the left-hand region of Fig. 1d). Moreover, inspired by the tristable conical Kresling [31] and inflatable multi-stable Kresling [24], here, we extend the concept of tristable Kresling bellows.

2.2.1 Tristability

A normal Kresling pattern folds along the long diagonals (crease pattern 1, see Fig. 3a) of each unit cell. If the geometric parameters are within the bistable region [5], it will therefore have two stable states (see Fig. 3b). Hereafter, we denote the more compressed state as S_1 and the more deployed state as S_2, with corresponding fold angles $\psi_1 < \psi_2$. Melancon et al. [24] introduced an additional crease along the short diagonal of a panel of a normal Kresling; during deployment, the panels initially remain planar until they suddenly snap radially outward, folding along the short diagonals, and the structure assumes a new stable state. Inspired by this idea, we introduce additional creases along the short diagonals for all panels (crease pattern 2, see Fig. 3a). If the structure can fulfil the geometric compatibility (Eqs. 3–5) when folding along crease pattern 2, the Kresling bellows will enter the third stable state (S_3), as shown in Fig. 3c. The third stable state involves an additional relative rotation of the cross sections and axial extension compared to the second stable state (S_2).

According to geometric constraints:

$$\frac{2H}{\tan(\phi_1)} + \frac{H}{\tan\left(\pi-\phi_1^{'}\right)} = \frac{H}{\tan(\phi_2)} \tag{11}$$

and thus, sector angles $\phi_1^{'}$ and $\phi_2^{'}$ of crease pattern 2 can be expressed as follows:

$$\phi_1^{'} = \arctan\left(\frac{\tan(\phi_1)\tan(\phi_2)}{2\tan(\phi_2)-\tan(\phi_1)}\right) \tag{12}$$

$$\phi_2^{'} = \phi_1 \tag{13}$$

where $\phi_1^{'} \in \left(\frac{\pi}{2}, \pi\right)$. For a compatible solution, $\phi_1^{'}$ and $\phi_2^{'}$ should satisfy the geometric constraints indicated in the right-hand region of Fig. 1d [5]. When $\phi_1^{'} \in \left(\frac{\pi}{2}, \frac{(n-1)\pi}{n}\right]$, the structures will always find solutions for state S_3; when $\phi_1^{'} \in \left(\frac{(n-1)\pi}{n}, \pi\right)$, sector angles should satisfy:

$$\phi_2^{'} > g_2\left(\phi_1^{'}, n\right) = \phi_1^{'} - \pi + \frac{\pi}{n} \tag{14}$$

For all Kresling patterns within the bistable region, it is found that a third compatible configuration S_3 exists.

2.2.2 Volume Calculation

In its folded configuration (see Fig. 4a), the geometry of the Kresling pattern can be described by height h_0, radius r, and

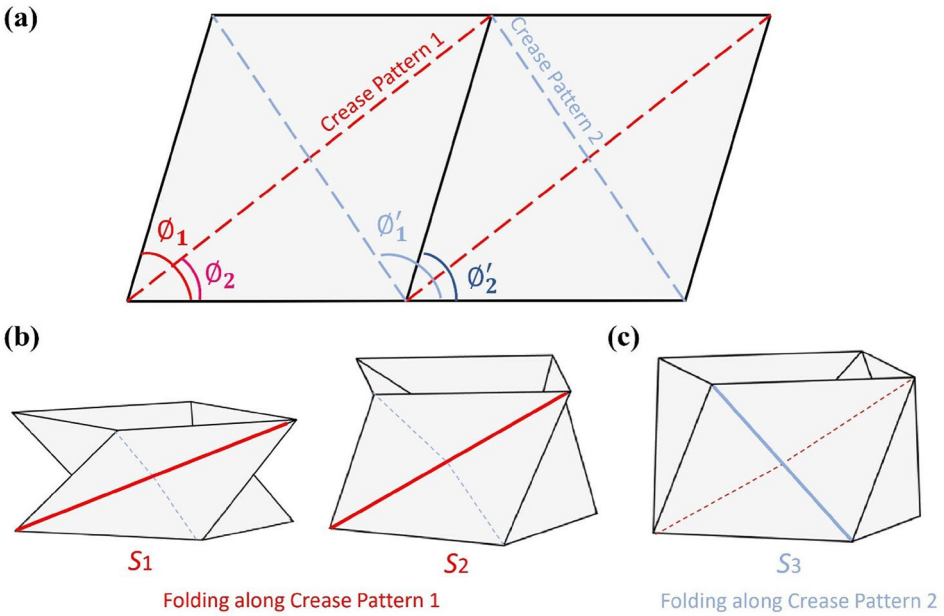

Fig. 3 Geometry of tristable Kresling bellows. **a** Illustration of the two Kresling crease patterns. The red dashed lines along the long diagonals indicate the primary pattern (pattern 1); the blue dashed lines along the short diagonals form the secondary crease (pattern 2) for the third stable state; ϕ_1 and ϕ_2 are sector angles of crease pattern 1, whilst $\phi_1^{'}$ and $\phi_2^{'}$ are sector angles of crease pattern 2. **b** 3D geometry for stable states S_1 and S_2 when folding along crease pattern 1 ($n = 4$, $\phi_1 = 77°$, $\phi_2 = 35°$). The thick red line is the active crease whilst the thin blue line represents an inactive crease (*i.e.*, no folding). **c** Corresponding 3D geometry at stable state S_3 when folding along crease pattern 2 ($\phi_1^{'} = 134°$, $\phi_2^{'} = 77°$). The thick blue line is the active crease whilst the thin red line represents an inactive crease

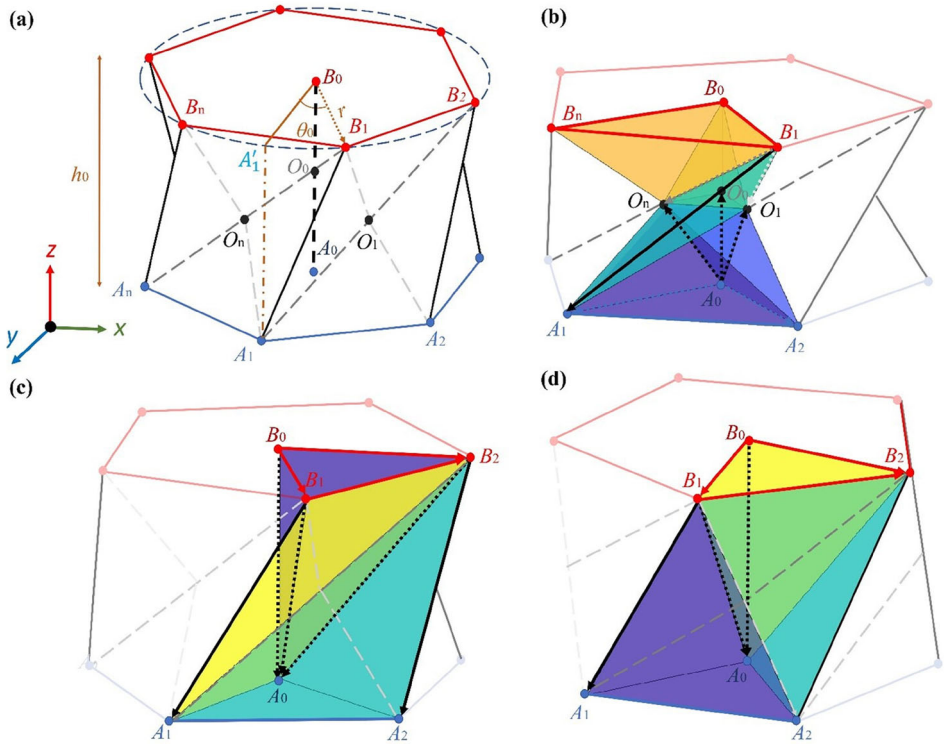

Fig. 4 3D Geometry of Kresling bellows and volume calculation of typical tristable Kresling bellows ($n = 5$, $m = 1$, $\phi_1 = 74°$,$\phi_2 = 41°$). A_0B_0 is the cylinder axis which is parallel to the z-axis, and O_0 is the midpoint of A_0 and B_0. The vectors used to calculate the volumes of the shaded tetrahedra (Eq. (24) and Eqs. (26)-(27)) are highlighted. Note that the viewing perspective is adjusted for each stable state. **a** 3D geometry of Kresling bellows in a stable state; the geometry can be described by initial height h_0, radius r, and initial rotation angle θ_0. **b** Seven constituent tetrahedra of a unit cell when O_1 penetrates tetrahedron $B_1B_2A_0A_1$ when folding along crease pattern 1 (state S_1). **c** Combination of three tetrahedra when O_1 does not penetrate tetrahedron $B_1B_2A_0A_1$ when folding along crease pattern 1 (state S_2). **d** Combination of three tetrahedra when folding along crease pattern 2 (state S_3)

initial rotation angle θ_0:

$$h_0 = H\cos\left(\frac{\pi}{2} - \psi\right) \tag{15}$$

$$r = \frac{d_1}{2\sin\left(\frac{\pi}{n}\right)} \tag{16}$$

$$\theta_0 = \arccos\left(\frac{2r^2 - A_1'B_1^2}{2r^2}\right) \tag{17}$$

Thus, the vertex coordinates can be expressed as follows:

$$A_0 = (0, 0, 0) \tag{18}$$

$$A_i = \left(r\cos\left(\frac{2\pi(i-1)}{n}\right), r\sin\left(\frac{2\pi(i-1)}{n}\right), 0\right) \tag{19}$$

$$B_0 = (0, 0, h_0) \tag{20}$$

$$B_i = \left(r\cos\left(\theta_0 + \frac{2\pi(i-1)}{n}\right), r\sin\left(\theta_0 + \frac{2\pi(i-1)}{n}\right), h_0\right) \tag{21}$$

where $i = 1, 2, \cdots, n$. The midpoint O_0 of axis A_0 and B_0 is given as follows:

$$O_0 = \left(0, 0, \frac{h_0}{2}\right) \tag{22}$$

And the intersection point O_i of crease pattern 1 and crease pattern 2 when folding along crease pattern 1 is calculated as follows:

$$O_i = \left(\frac{r\cos\left(\frac{2\pi(i-1)}{n}\right) + r\cos\left(\theta_0 + \frac{2\pi i}{n}\right)}{2}, \frac{r\sin\left(\frac{2\pi(i-1)}{n}\right) + r\sin\left(\theta_0 + \frac{2\pi i}{n}\right)}{2}, \frac{h_0}{2}\right) \tag{23}$$

for $i = 1, 2, \cdots, n$.

Since the Kresling pattern can be folded along either crease pattern 1 or crease pattern 2, it can be either a concave (Fig. 3b) or convex (Fig. 3c) when folded; therefore, the volume calculation method for S_3 is different from that for S_1 and S_2. What is more, if the structure is highly compressed at S_1 or S_2, it will lead to another volume calculation method. Taking a typical tristable Kresling ($n = 5$, $\phi_1 = 74°$,$\phi_2 = 41°$) as an example: at S_1, it is highly compressed (Fig. 4b), and the smallest repetitive unit ($B_0B_1B_nO_0O_1O_nA_1A_0A_2$) can be regarded as a combination of seven tetrahedra; at S_2, it deploys, and each unit can be partitioned into three tetrahedra (Fig. 4c); at S_3, the short diagonals (*e.g.*, B_1A_2) pop out radially (Fig. 4d), the structure becomes convex, and the unit cell is composed of three tetrahedra. The volume of the Kresling bellows at different stable states can then be calculated as follows:

First, consider the two different possibilities for the volume calculation when folding along crease pattern 1 to form states S_1 and S_2:

(i) If O_1 penetrates tetrahedron $B_1B_2A_0A_1$, the smallest repetitive unit can be divided into the seven tetrahedra ($A_0A_1A_2O_n$, $A_0A_2O_1O_n$, $A_0O_0O_1O_n$, $B_0B_1B_nO_n$, $B_0B_1O_1O_n$, $B_0O_0O_1O_n$, and $B_1A_1O_1O_n$) shown in Fig. 4b. Noting that $V_{A_0A_1A_2O_n} = V_{B_0B_1B_nO_n}$, $V_{A_0A_2O_1O_n} = V_{B_0B_1O_1O_n}$, and $V_{A_0O_0O_1O_n} = V_{B_0O_0O_1O_n}$, the total volume can be calculated as follows:

$$\begin{aligned} V_K = mn\Bigg(&\frac{1}{3}(\boldsymbol{A_0A_1}\times\boldsymbol{A_0A_2})\cdot\boldsymbol{A_0O_0} \\ &+\frac{1}{3}(\boldsymbol{A_0A_2}\times\boldsymbol{A_0O_1})\cdot\boldsymbol{A_0O_n} \\ &+\frac{1}{3}(\boldsymbol{A_0O_0}\times\boldsymbol{A_0O_1})\cdot\boldsymbol{A_0O_n} \\ &+\frac{1}{6}(\boldsymbol{B_1A_1}\times\boldsymbol{B_1O_1})\cdot\boldsymbol{B_1O_n}\Bigg) \end{aligned} \tag{24}$$

Substituting Eq. (18) into the above expression:

$$\begin{aligned} V_K = mnr^2h_0\Bigg\{&\frac{1}{6}\sin\left(\frac{2\pi}{n}\right) + \frac{1}{12}\Bigg[\sin\left(\theta_0 - \frac{2\pi}{n}\right) - \sin(\theta_0) \\ &+\sin\left(\frac{2\pi(n-2)}{n}\right) + \sin\left(\frac{2\pi}{n}\right)\Bigg] \\ &+\frac{1}{16}\Bigg[\sin(\theta_0) - \sin\left(\frac{4\pi}{n} - 2\pi + \theta_0\right) \\ &+\sin\left(\frac{2\pi(n-1)}{n}\right) + \sin\left(\frac{2\pi}{n}\right)\Bigg]\Bigg\} \end{aligned} \tag{25}$$

(ii) If O_1 does not penetrate tetrahedron $B_1B_2A_0A_1$, every single unit can be divided into the three tetrahedra ($B_0B_1B_2A_0$, $B_1B_2A_0A_1$ and $B_2A_0A_1A_2$) shown in Fig. 4c. Similarly, the total volume can be expressed as follows:

$$\begin{aligned} V_K &= mn\Bigg(\frac{1}{6}(\boldsymbol{B_0B_1}\times\boldsymbol{B_0B_2})\cdot\boldsymbol{B_0A_0} \\ &\quad+\frac{1}{6}(\boldsymbol{B_1B_2}\times\boldsymbol{B_1A_0})\cdot\boldsymbol{B_1A_1} \\ &\quad+\frac{1}{6}(\boldsymbol{B_2A_0}\times\boldsymbol{B_2A_1})\cdot\boldsymbol{B_2A_2}\Bigg) \\ &= mnr^2h_0\Bigg(\frac{2}{3}\sin\left(\frac{\pi}{n}\right)\cos\left(\frac{\pi}{n}\right) \\ &\quad+\frac{1}{6}\left|\sin(\theta_0) - \sin\left(\theta_0 + \frac{2\pi}{n}\right)\right|\Bigg) \end{aligned} \tag{26}$$

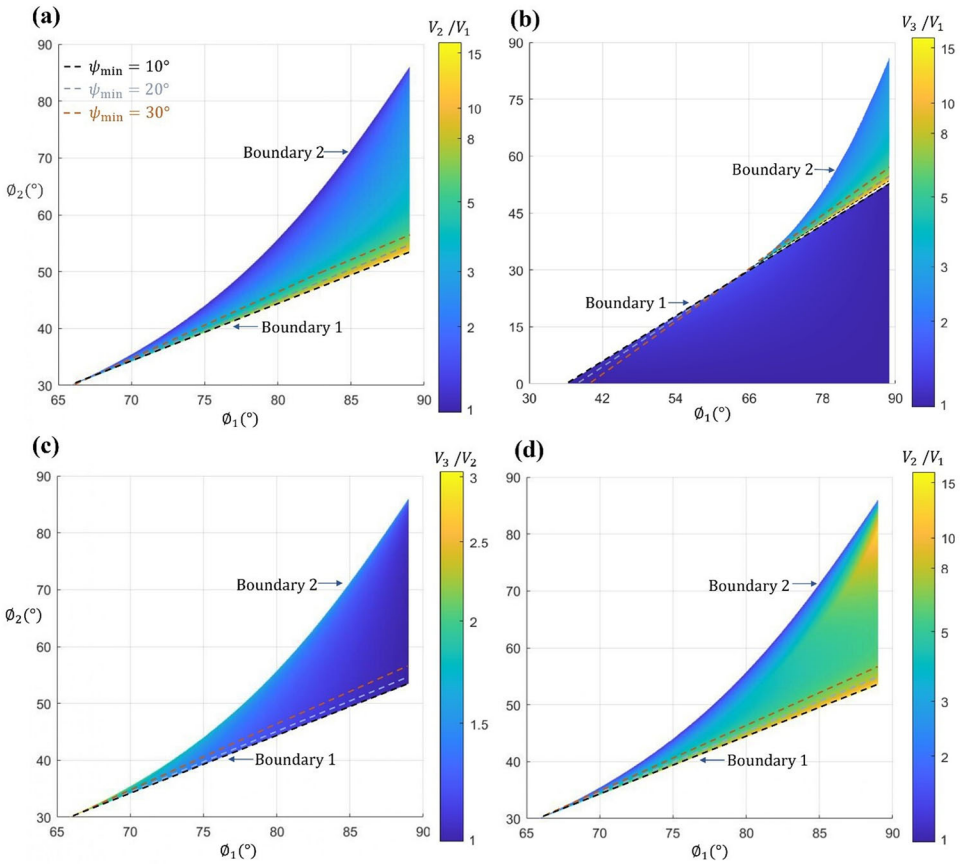

Fig. 5 Volume ratios of Kresling bellows ($n = 5$, $m = 1$, $\phi_1 \in [0°, 89°]$, $\phi_2 \in [0°, 89°]$) and Miura-ori bellows ($H/R = 2/3$) at different stable states in the design space, with minimum stowed angle $\psi_{min} = 10°$, 20°, and 30° indicated. V_1, V_2, V_3 represent the internal volumes at stable states S_1, S_2, and S_3, respectively. All volume ratios are greater than one, indicating the volume increases for different stable states during the deployment. With the increase in ψ_{min}, the feasible design space becomes smaller at boundary 1. **a** Kresling V_2/V_1, the ratio increases near boundary 1 with the increase in ϕ_1. **b** Kresling V_3/V_1, the ratio in the region above boundary 1 is much greater than the region below it; the ratio increases along boundary 1 with increasing ϕ_1. **c** Kresling V_3/V_2, the ratio is relatively large at boundary 2. **d** Miura-ori V_2/V_1, the ratio is largest along boundary 1 and for $\phi_1 = \pi/2$

Next, to calculate the volume at stable state S_3, each unit can be divided into the three tetrahedra ($B_0B_1B_2A_0$, $B_1A_0A_1A_2$, and $B_1B_2A_0A_2$) shown in Fig. 4d. Thus, the total volume is calculated as follows:

$$\begin{aligned} V_K &= mn\left(\frac{1}{6}(\boldsymbol{B_0B_1}\times\boldsymbol{B_0B_2})\cdot\boldsymbol{B_0A_0}\right.\\ &\quad+\frac{1}{6}(\boldsymbol{B_1A_0}\times\boldsymbol{B_1A_1})\cdot\boldsymbol{B_1A_2}\\ &\quad\left.+\frac{1}{6}(\boldsymbol{B_1B_2}\times\boldsymbol{B_1A_0})\cdot\boldsymbol{B_1A_2}\right)\\ &= mnr^2h_0\left(\frac{2}{3}\sin\left(\frac{\pi}{n}\right)\cos\left(\frac{\pi}{n}\right)\right.\\ &\quad\left.+\frac{1}{6}\left|\sin(\theta_0)-\sin\left(-\theta_0+\frac{2\pi}{n}\right)\right|\right) \end{aligned} \tag{27}$$

Equations (26) and (27) have the same first item since they both contain two tetrahedra whose base is $A_0A_1A_2$ or $B_0B_1B_2$ and has a height of h_0.

2.3 Volume Change of Multi-stable Origami Bellows

Figure 5 shows the volume change of Kresling and Miura-ori bellows between different stable states across the feasible geometric design space [5]. In practical applications, the bellows cannot be folded flat due to the thickness of the material; therefore, we set a minimum stowed angle ψ_{min} as a simple way to account for the panel thickness. Setting a minimum stowed angle will slightly reduce the feasible design space.

For the Kresling pattern, Fig. 5a and b indicates that both V_2/V_1 and V_3/V_1 increase near boundary 1 ($g_1(\phi_1, n)$ when $\psi > \psi_{min}$) with increasing ϕ_1. Figure 5b also shows that V_3/V_1 is comparatively small in the region below boundary 1. Moreover, the volume change between state S_3 and state S_2 (V_3/V_2) is overall not significant (Fig. 5c), but the ratio is relatively large at boundary 2 ($f(\phi_1, n)$ when $\psi > \psi_{min}$). Similar to Kresling, for Miura-ori, V_2/V_1 is the largest along boundary 1 and $\phi_1 = \pi/2$, as depicted in Fig. 5d. It is worth noting that increasing ψ_{min} reduces the feasible design space at boundary 1.

It can be observed from Fig. 5 that all volume ratios (V_2/V_1, V_3/V_1 and V_3/V_2) are greater than one, suggesting that the bellows' internal volume increases monotonically during the deployment. This finding makes Kresling and Miura-ori bellows suitable for inflatable structures and space habitats deployed through pressurisation. In the next section, we shall explore the application of these origami bellows for deployable space habitats, which will require additional calculations to determine the effective internal volume as well as the volume required to transport the stowed bellows.

3 Optimisation of Inflatable Origami Bellows for Space Habitats

Cylindrical origami such as Kresling and Miura-ori is suitable candidates for self-folding inflatable structures since the structure itself serves as the inflatable chamber. A potential application of such inflatable cylindrical origami structures is as deployable space habitats, which are stowed compactly during launch before expanding in orbit to offer additional working and living space.

In this section, we study and optimise the deployment ratio (expanded/stowed volume) and radial expansion ratio for cylindrical origami structures. First, we briefly introduce the background and design constraints for the proposed origami space habitats. Next, we outline the concepts of stowed volume and effective deployed volume of the origami bellows, which enable fair comparison with conventional habitat designs. Finally, crease patterns are sought to maximise the deployment ratio of origami space habitats using particle swarm optimisation (PSO). Lastly, multi-objective PSO (MOPSO) is adopted to balance the trade-off between deployment ratio and radial expansion ratio for bellows based on the Miura-ori pattern.

3.1 Design Background

The dimensions of the rocket fairing used to transport the habitat to space are an important factor in the selection of an origami pattern and geometry; specifically, the aspect ratio determines the number of layers m that can be stacked. Here, we take the SpaceX Falcon 9 [32] as an illustrative example; its payload fairing measures approximately 4.5 m in diameter and 6.7 m in height [33]. Allowing for some margin, we take radius $R_{\text{fairing}} = 2.2$ m and height $H_{\text{fairing}} = 6.5$ m as upper limits for our stowed module dimensions, which defines the available volume V_f of the fairing. Note that the aspect ratio $H_{\text{fairing}}/R_{\text{fairing}}$ rather than the actual dimensions matters, since the geometry of the origami bellows can be simply scaled. Moreover, this preliminary study is based purely on geometric considerations; the thickness of the module walls is considered by setting a minimum stowed angle $\psi_{\min}$. Other considerations such as materials selection, specific design of the bulkhead, the connection between the bulkhead, and the rest of the module as well as the internal support structure of the module are not involved here.

3.2 Effective Volume Calculation

The internal and external geometry of origami bellows are irregular-shaped (as depicted in Figs. 2 and 4) compared to conventional habitat modules. To account for this and enable fair comparisons, we define a *stowed volume* V_s and an *effective deployed volume* V_d for the origami bellows.

Stowed volume V_s: the volume of the smallest cylinder that completely encloses the bellows in the stowed configuration S_1. For both Kresling and Miura-ori bellows (Fig. 6a–i and b–i), V_s can be calculated as follows:

$$V_s = m\pi R_s^2 H_s \tag{28}$$

where H_s is the stowed height of a single layer, R_s is the radius of the circumscribed circle, which can be calculated by measuring the distance between A_0 and the projection of A_1 on the xy plane.

Effective deployed volume V_d: the volume of an unobstructed prism contained by the innermost fold lines of the bellows at deployed configurations S_2 or S_3 (see the blue shaded areas in Fig. 6).

For Kresling at S_2, as shown in Fig. 6a–ii:

$$V_d = nmA_0C_1^2 \sin\left(\frac{\pi}{n}\right)\cos\left(\frac{\pi}{n}\right)H_d \tag{29}$$

where H_d is the deployed height of a single layer, C_1 is the intersection point of the projections of line A_1B_2 and line A_2B_3 on the xy plane.

For Kresling at S_3, as shown in Fig. 6a–iii:

$$V_d = nm\sqrt{P_K(P_K - A_0C_1)(P_K - A_0D_1)(P_K - C_1D_1)}H_d \tag{30}$$

where C_1 is the intersection point of the projections of line A_1A_2 and line B_1B_2 on the xy plane, D_1 is the intersection point of the projections of line A_2A_3 and line B_1B_2 on the xy plane, and $P_K = \frac{1}{2}(A_0C_1 + A_0D_1 + C_1D_1)$.

For Miura-ori, when the projections of line A_2B_2 and line A_4B_4 have no intersection point on the xy plane (cross section type 1, see Fig. 6b–ii):

$$\begin{aligned} V_d = nm\Big(&\sqrt{P_{M1}(P_{M1} - A_0A_2)(P_{M1} - A_0B_2)(P_{M1} - A_2B_2)} \\ &+2\sqrt{P_{M2}(P_{M2} - A_0B_2)(P_{M2} - A_0C_1)(P_{M2} - B_2C_1)}\Big) \end{aligned} \tag{31}$$

where C_1 is the intersection point of the projections of A_3A_4 and B_2B_3 on the xy plane, $P_{M1} = \frac{1}{2}(A_0A_2 + A_0B_2 + A_2B_2)$, and $P_{M2} = \frac{1}{2}(A_0B_2 + A_0C_1 + B_2C_1)$. For Miura-ori, when the projections of line A_2B_2 and line A_4B_4 have an intersection point on the xy plane (cross section type 2, see Fig. 6b–iii):

$$V_d = nmA_0C_1^2 \sin\left(\frac{\pi}{n}\right)\cos\left(\frac{\pi}{n}\right)H_d \tag{32}$$

where C_1 is the intersection point of the projections of A_2B_2 and A_4B_4 on the xy plane.

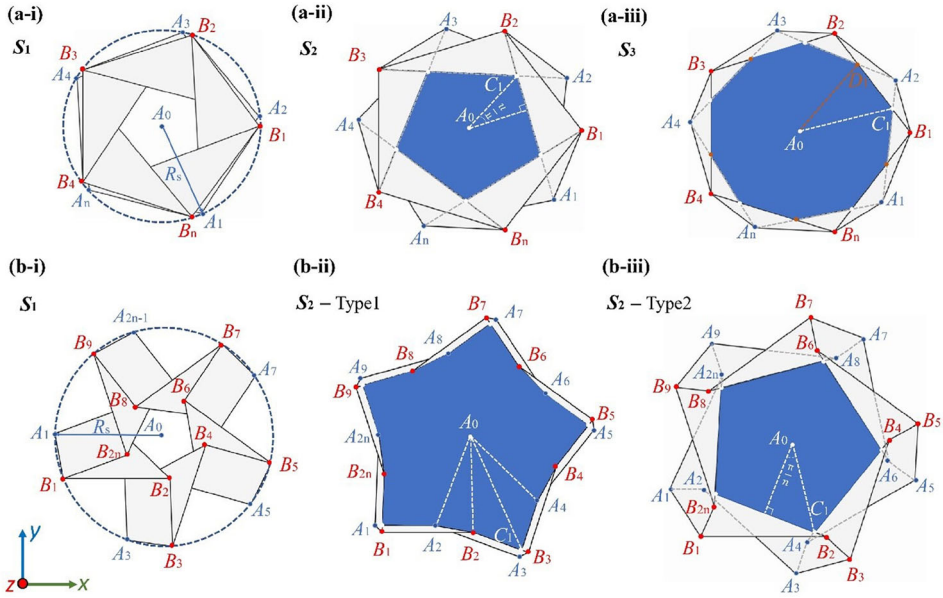

Fig. 6 Cross sections of Kresling and Miura-ori patterned bellows at different stable states. The facets are depicted in grey; the dashed blue circles are the circumscribed circles that completely enclose the bellows' cross section at S_1 with radius R_s; the blue shaded area is the cross section of the unobstructed prism contained by the innermost fold lines of the bellows at S_2 and S_3. **a-i** Kresling, cross section at S_1. **a-ii** Kresling, cross section at S_2. The dashed grey lines are projections of A_iB_j; C_1 is the intersection point of the projections of line A_1B_2 and line A_2B_3. **a-iii** Kresling, cross section at S_3. The dashed grey lines are projections of A_iA_j; C_1 is the intersection point of the projections of line A_1A_2 and line B_1B_2; D_1 is the intersection point of the projections of line A_2A_3 and line B_1B_2. **b-i** Miura-ori, cross section at S_1. **b-ii** Miura-ori, cross section at S_2 when the projections of A_2B_2 and A_4B_4 have an intersection point (Type 1); C_1 is the intersection point of the projections of A_3A_4 and B_2B_3. **b-iii** Miura-ori, cross section at S_2 when A_2B_2 and A_4B_4 have no intersection point (Type 2). The dashed grey lines are projections of A_iA_j; C_1 is the intersection point of the projections of A_2B_2 and A_4B_4

3.3 Definition of Optimisation Problem

The aim of the optimisation is to maximise the effective deployed volume of the structure that can be stowed in the payload fairing. Therefore, the ratio of the *effective deployed volume* (V_d) over the fairing volume (V_f),V_d/V_f, is chosen as the objective function. For Miura-ori patterns, the deployed volume is calculated at state S_2, whereas for the Kresling bellows, we utilise the volume at state S_3. This is motivated by the fact that V_3 is always greater than V_2 (see Fig. 5c), and that the axial stiffness at state S_3 was found to be up to several order of magnitude greater than at state S_2 and state S_1 for conical Kresling bellows [31].

Geometric parameters ϕ_1, ϕ_2, m, and n are selected as design variables, along with d_1/R for the Miura-ori pattern. The upper limit for ϕ_1 and ϕ_2 is set to be 85° to preclude structures that are too close to normal cylinders. The payload fairing height determines the integer number of layers m in the stowed configuration. Manufacturing considerations place limits on the maximum number of layers ($m = 8$) and circumferential unit cells ($4 \leq n \leq 8$). Larger values for m and n result in an increased number of panels, folds, and vertices, which will increase the manufacturing and assembly complexity of the origami bellows. The radius of the circumscribed cylinder R_s in the stowed configuration is set equal to the fairing radius R_{fairing}. A minimum dihedral angle $\psi_{\min} = 20°$ is used to account for the thickness of the panels in the stowed configuration, which is a constraint for the optimisation problem. Moreover, the fold pattern geometry should also lie in the feasible design region bounded by Eqs. (7)-(9). The constraints are handled using the static penalty function method [34], with the static penalty factor p selected as 10^5 here.

The optimisation design problem can thus be formulated as follows:

$$\text{maximise } V_d/V_f$$

$$s.t. \begin{cases} 0^\circ \leq \phi_1 \leq 85^\circ \\ 0^\circ \leq \phi_2 \leq 85^\circ \\ 1 \leq m = H_{\text{fairing}}/H_s \leq 8 \\ 4 \leq n \leq 8 \\ 0 < d_1/R < 2\pi/n \quad (\text{forMiura} - \text{oripattern}) \\ \psi \geq \psi_{\min} = 20^\circ \end{cases} \tag{33}$$

For the Miura-ori pattern, the structure will experience radial expansion during the deployment, which will bring challenges for the design of the bulkhead section at the ends

Table 1 Parameter settings for PSO and MOPSO

Parameters	Value (PSO)	Value (MOPSO)
Population size	3000	3000
Number of generations for Kresling	1500	–
Number of generations for Miura-ori	500	500
Inertia weight ω	1.0	1.0
Inertia weight damping ratio ω_{damping}	0.99	0.99
Personal learning factor C_1	1.5	1.5
Global learning factor C_2	2.0	2.0
Mutation rate	–	0.1
Repository size	–	100

of the structure (*e.g.,* maintaining air tightness and ensuring smooth deployment). Therefore, the radial expansion (R_d/R_s) should also be considered, leading to a multi-objective optimisation problem:

$$\text{minimise } (-V_d/V_f,\, R_d/R_s)$$
$$s.t. \begin{cases} 0^\circ \le \phi_1 \le 85^\circ \\ 0^\circ \le \phi_2 \le 85^\circ \\ 1 \le m = H_{\text{fairing}}/H_s \le 8 \\ 4 \le n \le 8 \\ 0 < d_1/R < 2\pi/n \\ \psi \ge \psi_{\min} = 20^\circ \end{cases} \tag{34}$$

Note that for multi-objective optimisation, the deployed volume is necessarily calculated at state S_2, even if the design parameters approach those of a Kresling pattern.

3.4 Optimisation Algorithm

The PSO [35] and MOPSO [36] algorithms are utilised for single-objective and multi-objective optimisation, respectively. Details of the algorithms are provided in Appendix A. The algorithm parameters are selected according to [35, 36] and adjusted for the optimisation problem listed in Table 1.

3.5 Results and Discussion

3.5.1 Single-Objective Optimisation

The geometric parameters of the optimal designs are listed in Table 2, and the corresponding stowed and deployed configurations are presented in Fig. 7. The Convergence histories are illustrated in Appendix B. For the Kresling pattern, the achieved volume ratio $V_d/V_f = 2.56$, whilst maintaining a constant cross sectional area. The increase in volume is therefore due to the change in height from 0.81 m per layer in the stowed state to 2.37 m in the deployed configuration. In the case of the Miura-ori pattern, in addition to the increase in height, the structure also shows a significant radial expansion during the deployment ($R_d/R_s = 1.84$). Thus, the Miura-ori pattern can achieve much more significant volumetric expansion ($V_d/V_f = 8.31$). It is interesting to observe that the optimal designs of these two patterns have the same number of layers, and the same stowed and deployed heights. Furthermore, both patterns utilise the maximum number of unit cells $n = 8$. This can be explained by the exploration of the influence of n, which shows a trend of increasing volume with increasing n (see Appendix C). Lastly, the values for ϕ_1 and ϕ_2 are close to the flat-foldable region ($g_1(\phi_1, n) = \phi_1 - \pi/n$), minimising the height of the stowed configuration. Relaxing constraints on the panel thickness and number of unit cells could further increase the effective volume. Appendix D shows the optimal results for different values of n and $\psi_{\min}$.

3.5.2 Multi-Objective Optimisation

The Pareto front for the multi-objective optimisation is shown in Fig. 8a. It is not continuous since the design parameters m and n are integers, and the objective function is highly nonlinear. Evidently, the two objectives $-V_d/V_f$ and R_d/R_s are in strong competition with each other. The optimal design is normally chosen from the Pareto-optimal set according to the designers' requirements, such as assigning weights for objectives.

The results of the corresponding single-objective optimisation (SOO) should lie at the extremes of the Pareto-optimal set. The top-left solution (pointed out in Fig. 8a) on the Pareto front is also the optimal result for Miura-ori obtained in Sect. 3.5.1. The bottom-right solution should be the optimal result for Miura-ori with the objective of minimising R_d/R_s. The ratio R_d/R_s will reach its minimum ($R_d/R_s = 1$) when the Miura-ori reduces to the Kresling pattern. Thus, the bottom-right solution should be the SOO result for minimising $-V_d/V_f$ for the Kresling pattern that sets S_2 as the deployed state (solid purple square, $-V_d/V_f = -2.14$, $R_d/R_s = 1.00$). However, the optimiser fails to precisely find that SOO result. This can be explained by the fact that the optimiser will easily fall into local minima when it approaches any configuration that is close to the Kresling pattern ($d_1/R = 2\pi/n$, $d_2 = 0$), since for every Kresling pattern, $R_d/R_s = 1$. Nonetheless, the optimiser has nominally found the single-objective solutions for both ends of the design space and provided a Pareto front to enable the selection of designs that balance the objectives. Here, to limit the radial expansion ratio and ensure a reliable result, we select an optimal design with a radial expansion ratio $R_d/R_s \le 1.5$,

Table 2 Design variables of optimal designs

Algorithm	Pattern	$\phi_1(^\circ)$	$\phi_2(^\circ)$	m	n	d_1/R	H_s(m)	H_d(m)	R_d/R_s	V_d/V_f
PSO	Kresling	60.36	38.02	8	8	–	0.81	2.37	1	2.56
	Miura-ori	85	63.63	8	8	0.52	0.81	2.37	1.84	8.31
MOPSO	Miura-ori	85	60.69	6	7	0.67	1.08	2.97	1.50	4.90

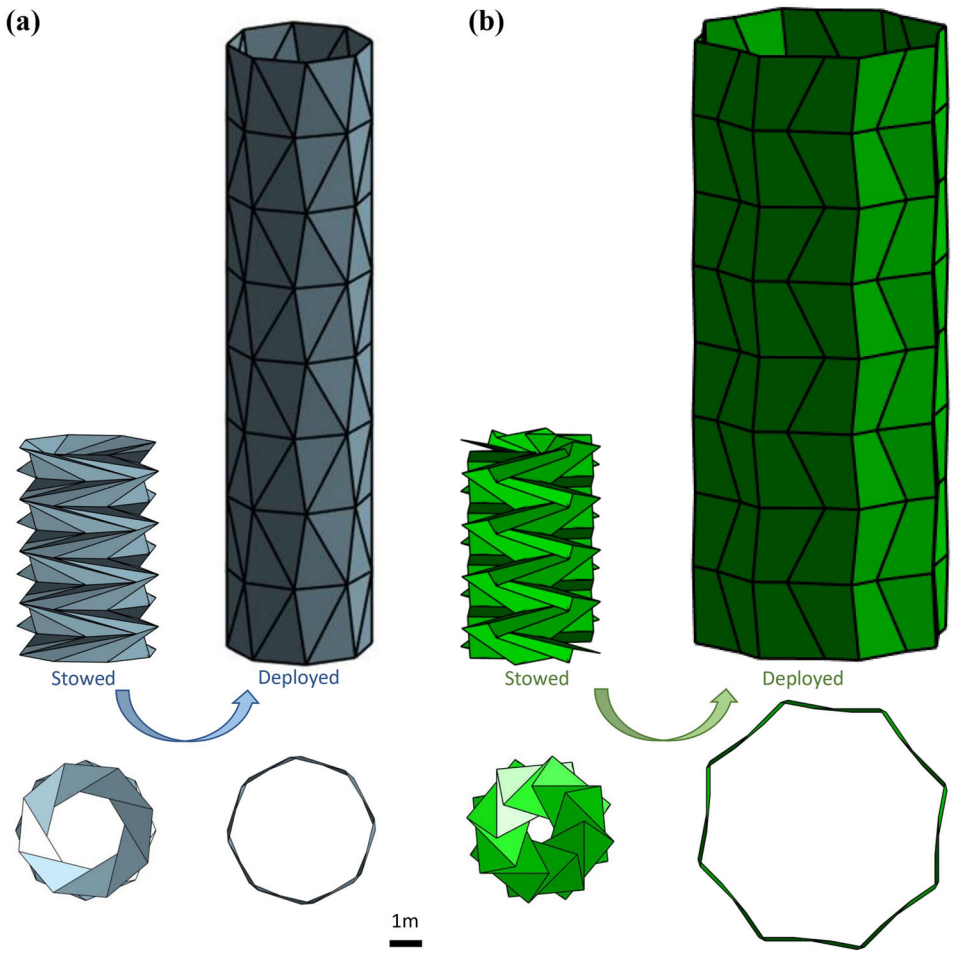

Fig. 7 Stowed and deployed configurations of optimal designs obtained by PSO; only active creases are shown. The stowed Kresling and Miura configurations conform to the same fairing dimensions. **a** Kresling pattern ($n = 8$, $m = 8$, $\phi_1 = 60.36^\circ$, $\phi_2 = 38.02^\circ$, $R = 2.14$ m, $V_d/V_f = 2.56$). The cross sectional area remains unchanged during deployment, and the increase in volume is thus due to the change in height. **b** Miura-ori pattern ($n = 8$, $m = 8$, $\phi_1 = 85^\circ$, $\phi_2 = 63.63^\circ$, $d_1/R = 0.52$, $R = 3.96$ m, $V_d/V_f = 8.31$, $R_d/R_s = 1.84$). In addition to the increase in height, the structure also shows significant radial expansion ($R_d/R_s = 1.84$) during deployment, resulting in improved volume expansion

marked with an asterisk in Fig. 8a. The geometric parameters of the optimal design are listed in Table 2, and the stowed and deployed configurations of the optimal design are depicted in Fig. 8b.

4 Conclusions

In this paper, we investigate the volume of multi-stable origami bellows in their compatible configurations. The full geometric design space of bistable Miura-ori and tristable Kresling bellows is explored. The internal volume of the structures is shown to increase between different stable states during the deployment procedure, meaning that these bellows can be utilised as inflatable self-folding structures.

The application as a deployable space habitat is explored; the cylindrical origami structure would be stowed during launch in one stable configuration before expanding to an extended configuration in orbit. In order to enable fair comparison with conventional habitats, we define the stowed volume and effective deployed volume of the origami habitat. The dimensions of the SpaceX Falcon 9 payload fairing are used as a case study. Using a particle swarm optimisation (PSO) method, patterns are found that maximise the volume deployment ratio (effective deployed volume over stowed volume) of the origami habitat. The results show that the Kresling pattern can achieve a volume expansion ratio of 2.56, whilst the Miura-ori pattern can reach a ratio of 8.31, offering significant volume increases compared to a conventional cylindrical habitat. However, the radial expansion of

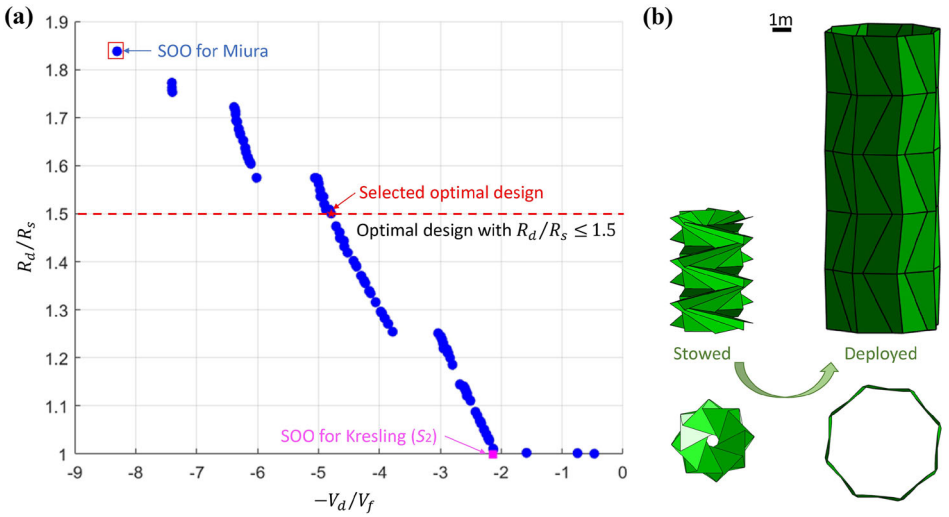

Fig. 8 Optimal result of MOPSO for Miura-ori pattern bellows, trading off the change in deployed volume against the change in deployed radius. **a** Pareto-optimal front. The two objectives strongly compete with each other. The top-left solution on the Pareto front is also the result of the single-objective optimisation (SOO) for the Miura-ori pattern; the solid purple square represents the SOO result for minimising $-V_d/V_f$ for the Kresling pattern, setting S_2 as the deployed state. An optimal design is selected by setting the radial expansion ratio $R_d/R_s \leq 1.5$, as represented by a red dashed line and marked by an asterisk. **b** The stowed and deployed configurations of the selected optimal design ($n = 8$, $m = 5$, $\phi_1 = 85°$, $\phi_2 = 63.66°$, $d_1/R = 0.60$, $R = 3.23$ m, $-V_d/V_f = -4.79$, $R_d/R_s = 1.50$)

the Miura-ori bellows will bring significant challenges for the design of the bulkhead section at the ends of the structure. Multi-Objective PSO is therefore used to balance the volume and radial expansion, allowing a final design to be selected from the Pareto front.

The current study is a strictly geometric analysis of origami bellows for space habitats. Panel thickness (for thermal insulation, radiation protection, debris shielding, etc.) has not been considered, and practical designs would require careful consideration of the folds and vertices to enable compact stowage whilst maintaining air tightness. Furthermore, the structural mechanics has not yet been considered either for modelling the deployment (which requires panel bending and stretching) or the performance of the final deployed structure. Considering the various complexities in design and fabrication, it is at present difficult to assess whether origami-inspired space habitats are a worthwhile pursuit. Nonetheless, the present study shows that such deployable origami structures could offer a significant increase in habitat volume compared to conventional habitats for the same fairing dimensions. Moreover, the proposed multi-objective optimisation framework can be extended to include additional considerations for the design of optimal patterns for origami space habitats and other engineering origami applications.

Acknowledgements Mengzhu Yang is supported through a China Scholarship Council (CSC)–University of Bristol joint scholarship.

Data Availability All data required to reproduce the results are contained within the paper.

Declarations

Conflict of interest The authors declare that they have no known competing financial interests or personal relationships that could have appeared to influence the work reported in this paper.

Appendix A: Optimisation Algorithms

PSO is a bio-inspired method purposed by Kennedy and Eberhart [35] to simulate the social behaviours in a bird flock or fish school. It has been successfully used in the optimal design of non-trivial flat-foldable origami patterns [37]. The optimisation toolbox used in this paper is from Heris [38].

Particles are firstly initialised to be randomly distributed in the design space with velocity $V_i(t)$ and position $P_i(t)$. Next, the velocity vector and position of each particle are updated based on its own experience P_{pbest} and its neighbours' experience P_{gbest} according to the following equations [35, 38]:

$$V_i(t+1) = \omega(t+1) \cdot V_i(t) + C_1 \cdot \text{rand}() \cdot \left(P_{\text{pbest}} - P_i(t)\right) + C_2 \cdot \text{rand}() \cdot \left(P_{\text{gbest}} - P_i(t)\right) \tag{A.1}$$

$$P_i(t+1) = P_i(t) + V_i(t+1) \tag{A.2}$$

where $V_i(t)$ and $P_i(t)$ represent the velocity and position of the particle at iteration t, C_1 and C_2 are the personal and global learning parameters, rand() is a random value in the interval [0,1], P_{pbest} is the best solution thus far, P_{gbest} is the best particle in the entire swarm, and $\omega(t+1)$ is the inertia weight which controls the trade-off between global and local experience, which is calculated as follows:

$$\omega(t+1) = \omega(t)\, \omega_{\text{damping}} \tag{A.3}$$

where ω_{damping} is the inertia weight damping ratio.

Coello et al. [36] adapted PSO for a multi-objective optimisation problem by introducing a repository that stores the positions of the non-dominated particles. For multi-objective particle swarm optimisation (MOPSO), P_{pbest} and P_{gbest} are chosen from the repository.

Appendix B: Iteration Histories of Optimisation Algorithms

Figure 9 illustrates the convergence histories and corresponding geometry at typical iterations, demonstrating the increase in the function value and change of geometry towards the optimal design. The Miura-ori pattern converges earlier than the Kresling since it only seeks solutions with $\phi_1 = 85°$ as this results in the greatest expansion ratio (see Fig. 5).

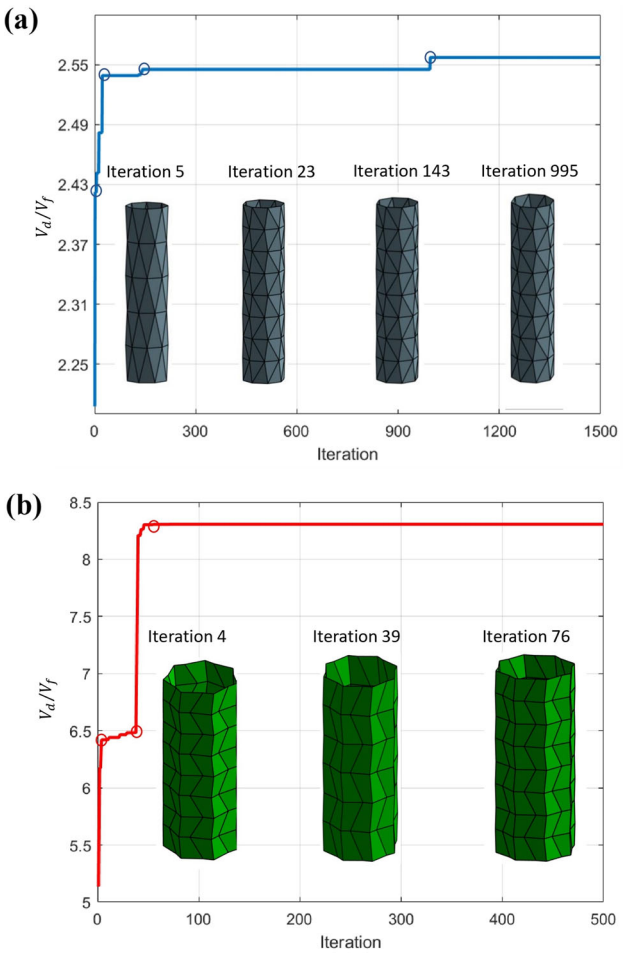

Fig. 9 Iteration histories and corresponding geometry at typical iterations, demonstrating the increase in the function value and change of geometry towards the optimal design. **a** Kresling pattern. **b** Miura-ori pattern. The optimiser only seeks solutions with $\phi_1 = 85°$

Appendix C: Influence of *n* on Effective Volume

Here, we explore the influence of the number of circumferential unit cells n on the effective volume of tristable Kresling bellows and bistable Miura-ori bellows. Figure 10 presents the effective volume at the most compressed stable state (V_1/V_s) and the most deployed stable state (V_d/V_3 or V_d/V_2) when n increases from 5 to 7 in the geometrically multi-stable design space. For both crease patterns, the effective volume shows an overall increase with increasing n. It is intuitive that

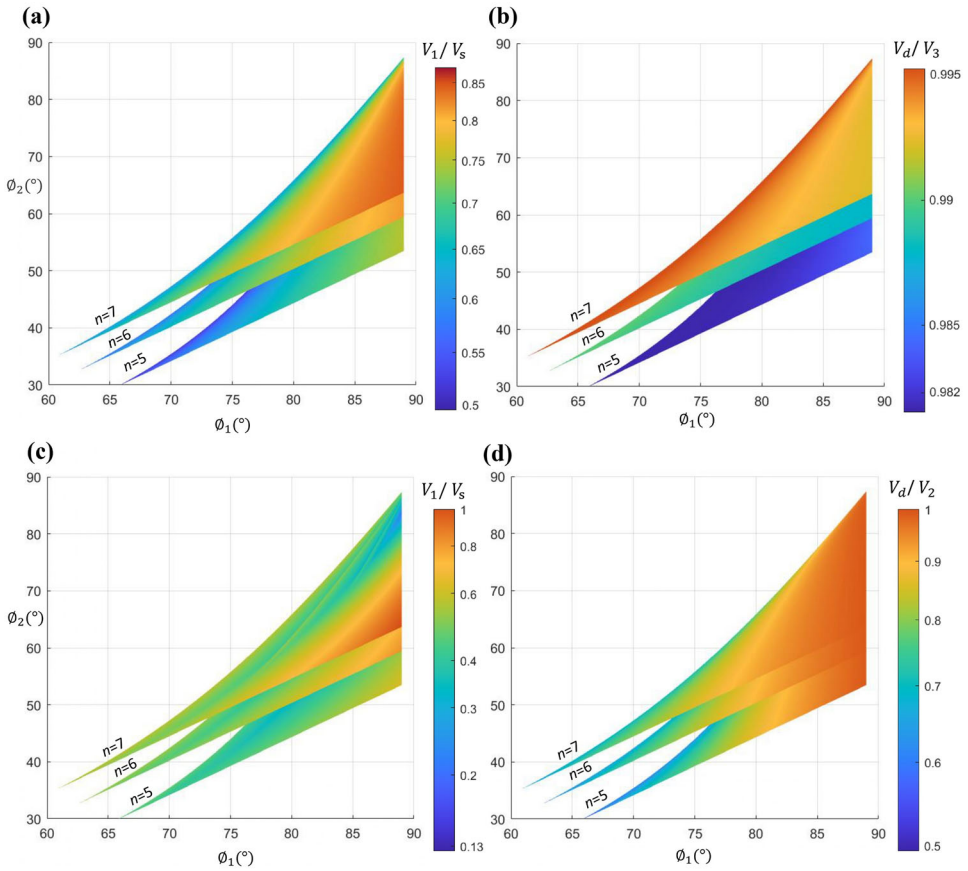

Fig. 10 Influence of n ($n = 5$, 6 and 7) on the effective volume of Kresling bellows ($m = 1$, $\phi_1 \in (0°, 89°)$, $\phi_2 \in (0°, 89°)$, $R = 40$ mm, $\psi > \psi_{\min} = 10°$), and Miura-ori bellows ($m = 1$, $\phi_1 \in (0°, 89°)$, $\phi_2 \in (0°, 89°)$, $R = 60$ mm, $H = 60$ mm, $\psi > \psi_{\min} = 10°$) at different stable states, showing an overall increase in the effective volume with the increase in n. Note that the colour bars indicate that base-10 logarithms of the volume ratios to effectively show a larger range. **a** Kresling, V_1/V_s. **b** Kresling, V_d/V_3. **c** Miura-ori, V_1/V_s. **d** Miura-ori, V_d/V_2

with the increase in n, the bellows more closely approximate smooth cylinders, leading to the increase in effective volume.

It can be observed from Fig. 10a and c that for both Kresling and Miura-ori bellows, V_1/V_s increases along the line closest to the flat-foldable line ($g_1(\phi_1, n) = \phi_1 - \pi/n$), and when ϕ_2 hits the upper bound, V_1/V_s reaches the maximum value.

For Kresling, V_d/V_3 shows a distinct overall increase when n ranges from 5 to 7. However, the range of V_d/V_3 is narrow (from 0.83 to 0.95), indicating that Kresling has an overall ideal effective volume at the most deployed state (S_3). The ratio is relatively large around the upper boundary of the bistable region $f(\phi_1, n) = \arctan((\tan\phi_1(1 - \sin(\pi/n))) / (1 + \sin(\pi/n)))$. In this region, the angle ψ (here $\psi > \pi/2$) is relatively small, resulting in structures that are close to the corresponding right prism, and eventually leading to a big effective volume. Similarly, for Miura-ori, when ϕ_2 increases, ψ will be closer to $\pi/2$ and thus, has a big effective volume.

Appendix D: Sensitivity to Design Variables' Constraints

The influence of the domain of design variables on optimal results is briefly studied in this section. In the main paper, manufacturing considerations set the minimum stowed angle at $\psi_{\min} = 20°$ and the number of circumferential unit cells at $n_{\max} = 8$. Here, we explore the influence of $\psi_{\min}$ and $n_{\max}$ on optimal designs. Table 3 shows the optimal results when $\psi_{\min} = 10°, 20°$ and $30°$, whilst maintaining $n_{\max} = 8$. With the increase in $\psi_{\min}$, the objective function value decreases since the feasible design space becomes smaller, as shown in Fig. 5. The Kresling pattern is more sensitive to the change of $\psi_{\min}$ than the Miura-ori pattern. Table 4 shows the optimal results when $n_{\max} = 8, 9$, and 10, while keeping $\psi_{\min} = 20°$. The table suggests that increasing $n_{\max}$ is an efficient method to obtain a large deployment ratio, especially for the Miura-ori pattern.

Table 3 Optimal designs with different $\psi_{\min}$

Pattern	$\psi_{\min}(^\circ)$	$\phi_1(^\circ)$	$\phi_2(^\circ)$	m	n	d_1/R	V_d/V_f
Kresling	10	85	62.89	8	8	–	4.28
	20	60.36	38.02	8	8	–	2.56
	30	83.02	62.93	3	8	–	1.74
Miura-ori	10	85	63.44	8	8	0.53	8.40
	20	85	63.63	8	8	0.52	8.31
	30	85	65.03	7	8	0.46	6.70

Table 4 Optimal designs with different $n_{\max}$

Pattern	$\psi_{\min}(^\circ)$	$\phi_1(^\circ)$	$\phi_2(^\circ)$	m	n	d_1/R	V_d/V_f
Kresling	8	60.36	38.02	8	8	–	2.56
	9	62.59	42.88	7	9	–	2.65
	10	67.04	49.50	6	10	–	2.72
Miura-ori	8	85	63.63	8	8	0.52	8.31
	9	85	66.04	8	9	0.45	10.21
	10	85	67.95	8	10	0.39	12.20

Appendix E: Software for Geometry and Volume Calculation for Miura-ori and Kresling Bellows

We have developed a MATLAB code [39] to generate the geometry and calculate the volume for multi-stable Miura-ori and Kresling bellows. The interface of the software is shown in Fig. 11. Users choose a crease pattern (Kresling or Miura-ori) and then, input design parameters (n, ϕ_1, ϕ_2, R, m and d_1/R for the Miura-ori pattern). The software will output the geometry at each feasible stable state and calculate the ratio of height change (H_dS_2/H_s, H_dS_3/H_s), radial expansion (R_dS_2/R_s, R_dS_3/R_s), internal volume change (V_2/V_1, V_3/V_1), and effective volume change (V_dS_2/V_s, V_dS_3/V_s). The geometry of the bellows in the stable states can be exported into the *fold* format.

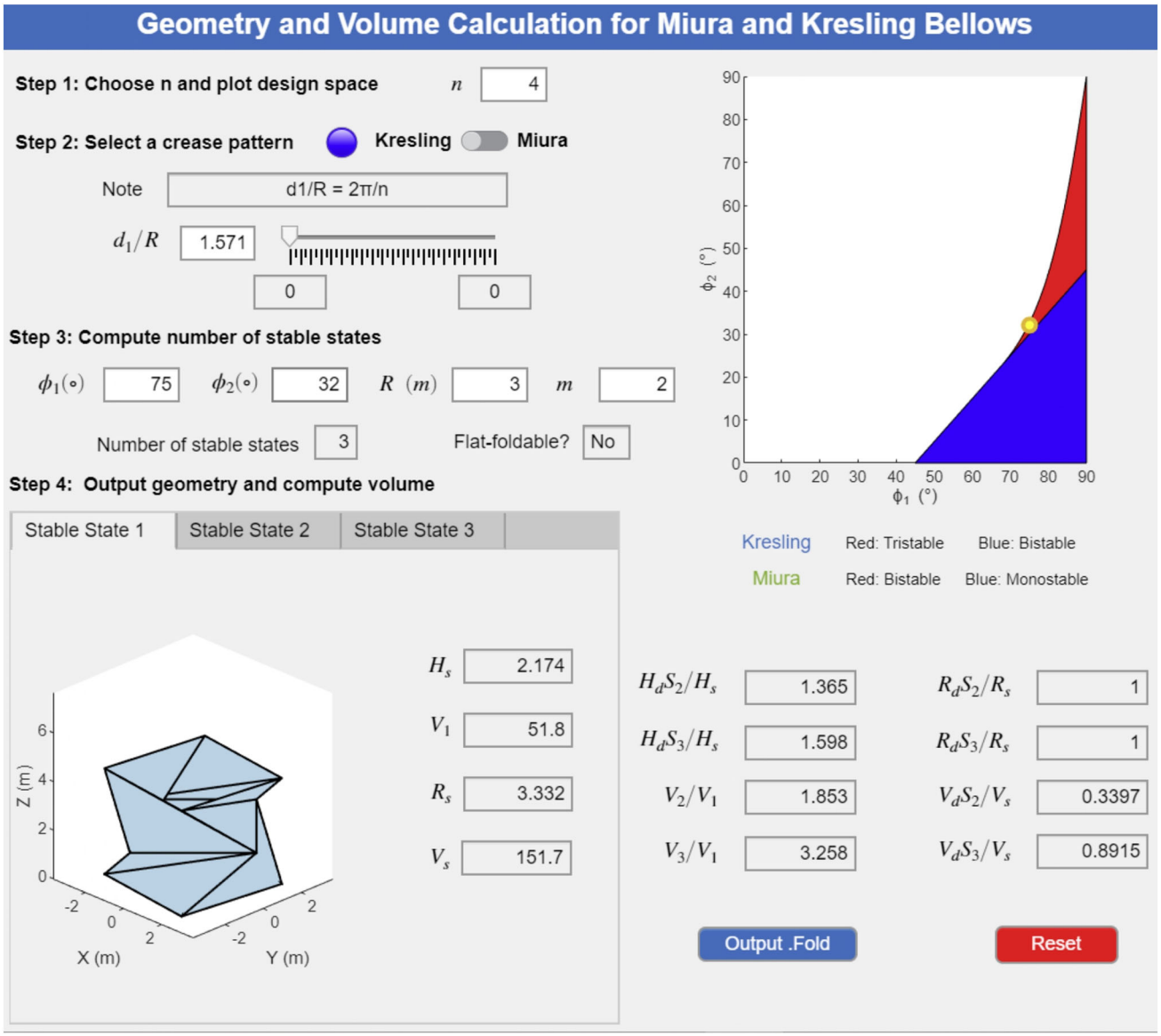

Fig. 11 Interface of the MATLAB code to generate the geometry and calculate the volume for multi-stable Miura-ori and Kresling bellows

References

1. Meloni M, Cai J, Zhang Q, Sang-Hoon LD, Li M, Ma R, Parashkevov TE, Feng J. Engineering origami: a comprehensive review of recent applications, design methods, and tools. Adv Sci. 2021;8(13):2000636.
2. Kuzyk A, Jungmann R, Acuna GP, Liu N. Dna origami route for nanophotonics. ACS Photon. 2018;5(4):1151–63.
3. Melancon D, Gorissen B, Garcıa-Mora CJ, Hoberman C, Bertoldi K. Multistable inflatable origami structures at the metre scale. Nature. 2021;592(7855):545–50.
4. Lu L, Leanza S, Zhao RR. Origami with rotational symmetry: A review on their mechanics and design. Appl Mech Rev. 2023;1–64.
5. Reid A, Lechenault F, Rica S, Adda-Bedia M. Geometry and design of origami bellows with tunable response. Phys Rev E. 2017;95(1):013002.
6. Kresling B. Plant, "design": mechanical simulations of growth patterns and bionics. Biomimetics. 1996;3:105–20.
7. Chen Y, Feng H, Ma J, Peng R, You Z. Symmetric waterbomb origami. Proc Royal Soc A Math Phys Eng Sci. 2016;472(2190):20150846.
8. Grasinger M, Gillman A, Buskohl PR. Multistability, symmetry and geometric conservation in eightfold waterbomb origami. Proc Royal Soc A. 2022;478(2268):20220270.
9. Masana R, Daqaq MF. Equilibria and bifurcations of a foldable paper-based spring inspired by kresling-pattern origami. Phys Rev E. 2019;100(6):063001.
10. Lu L, Dang X, Feng F, Lv P, Duan H. Conical kresling origami and its applications to curvature and energy programming. Proc Royal Soc A. 2022;478(2257):20210712.
11. Li Z, Kidambi N, Wang L, Wang KW. Uncovering rotational multifunctionalities of coupled kresling modular structures. Extreme Mechanics Letters. 2020;39:100795.
12. Zhai Z, Wang Y, Jiang H. Origami-inspired, on-demand deployable and collapsible mechanical metamaterials with tunable stiffness. Proc Natl Acad Sci. 2018;115(9):2032–7.

13. Mukhopadhyay T, Ma J, Feng H, Hou D, Gattas JM, Chen Y, You Z. Programmable stiffness and shape modulation in origami materials: Emergence of a distant actuation feature. Appl Mater Today. 2020;19:100537.
14. Suh JE, Miyazawa Y, Yang J, Han JH. Self-reconfiguring and stiffening origami tube. Adv Eng Mater. 2022;24(5):2101202.
15. Kaufmann J, Bhovad P, Li S. Harnessing the multistability of kresling origami for reconfigurable articulation in soft robotic arms. Soft Rob. 2022;9(2):212–23.
16. Onal CD, Wood RJ, Rus D. An origami-inspired approach to worm robots. IEEE/ASME Trans Mechatron. 2012;18(2):430–8.
17. Yamaguchi K, Yasuda H, Tsujikawa K, Kunimine T, Yang J. Graph-theoretic estimation of reconfigurability in origami-based metamaterials. Mater Des. 2022;213:110343.
18. Kamrava S, Ghosh R, Wang Z, Vaziri A. Origami-inspired cellular meta-material with anisotropic multi-stability. Adv Eng Mater. 2019;21(2):1800895.
19. Masana R, Khazaaleh S, Alhussein H, Crespo R, Daqaq M. An origami-inspired dynamically actuated binary switch. Appl Phys Lett. 2020;117(8):081901.
20. Novelino LS, Ze Q, Wu S, Paulino GH, Zhao R. Untethered control of functional origami microrobots with distributed actuation. Proc Natl Acad Sci. 2020;117(39):24096–101.
21. Kim, Lee DY, Kim SR, Cho KJ. A self-deployable origami structure with locking mechanism induced by buckling effect. In: 2015 IEEE International Conference on Robotics and Automation (ICRA), IEEE;, 2015. p. 3166–71.
22. Fonseca LM, Savi MA. Nonlinear dynamics of an autonomous robot with deformable origami wheels. Int J Non-Linear Mech. 2020;125:103533.
23. Li S, Vogt DM, Rus D, Wood RJ. Fluid-driven origami-inspired artificial muscles. Proc Natl Acad Sci. 2017;114(50):13132–7.
24. Melancon D, Forte AE, Kamp LM, Gorissen B, Bertoldi K. Inflatable origami: multimodal deformation via multistability. Adv Funct Mater. 2022;13:2201891.
25. Zhang Z, Chen G, Wu H, Kong L, Wang H. A pneumatic/cable-driven hybrid linear actuator with combined structure of origami chambers and deployable mechanism. IEEE Robot Autom Lett. 2020;5(2):3564–71.
26. Schenk M, Viquerat AD, Seffen KA, Guest SD. Review of inflatable booms for deployable space structures: packing and rigidization. J Spacecr Rocket. 2014;51(3):762–78.
27. Morgan J, Magleby SP, Howell LL. An approach to designing origami adapted aerospace mechanisms. J Mech Des. 2016;138(5):052301.
28. Bigelow. Bigelow Expandable Activity Module (BEAM). https://www.bigelowaerospace.com/pages/beam/, accessed: 2023–02–15.
29. S. Space Architects, Lunark. https://saga.dk/projects/lunark/habitat, accessed: 2023–02–12.
30. Yasuda H, Gopalarethinam B, Kunimine T, Tachi T, Yang J. Origami-based cellular structures with in situ transition between collapsible and load-bearing configurations. Adv Eng Mater. 2019;21(12):1900562.
31. Wo Z, Filipov ET. Stiffening multi-stable origami tubes by outward popping of creases. Extreme Mech Lett. 2023;58:101941.
32. SpaceX, Falcon 9. https://www.spacex.com/vehicles/falcon-9, accessed: 2023–01–11.
33. SpaceX, Falcon User's Guide. https://www.spacex.com/media/falcon-users-guide-2021-09.pdf, accessed: 2023–01–11.
34. Liu J, Teo KL, Wang X, Wu C. An exact penalty function-based differential search algorithm for constrained global optimization. Soft Comput. 2016;20:1305–13.
35. Kennedy J, Eberhart R. Particle swarm optimization. In: Proceedings of ICNN'95-international conference on neural networks, Vol. 4, IEEE; 1995.p. 1942–8.
36. Coello CAC, Pulido GT, Lechuga MS. Handling multiple objectives with particle swarm optimization. IEEE Trans Evol Comput. 2004;8(3):256–79.
37. Chen Y, Yan J, Feng J, Sareh P. Particle swarm optimization-based metaheuristic design generation of non-trivial flat-foldable origami tessellations with degree-4 vertices. J Mech Des. 2021;143(1):011703.
38. Heris MK. Particle Swarm Optimization in Matlab. https://yarpiz.com/50/ypea102-particle-swarm-optimization, accessed: 2023–02–12.
39. MATLAB code for generating multi-stable Miura-ori and Kresling bellows. https://github.com/Mengzhu-Yang/Software_Geometry_and_-Volume_Calculation_for_Origami_Bellows.